Applied Clay Science 195 (2020) 105739

Contents lists available at ScienceDirect

Applied Clay Science

journal homepage: www.elsevier.com/locate/clay

Research Paper

# Clay saline diagenesis in lake Plio-Pleistocene sediments rich in organic matter from the Guadix-Baza Basin (Betic Cordillera, SE Spain)

Juan Jiménez-Millán[a,*], Isabel Abad[a], Francisco Juan García-Tortosa[a], Fernando Nieto[b], Rosario Jiménez-Espinosa[a]

[a] Department of Geology and CEACTEMA, IACT Associated Unit, University of Jaén. Campus Las Lagunillas, 23071 Jaén, Spain
[b] Department of Mineralogy and Petrology and IACT, University of Granada-CSIC, Fuentenueva s / n, 18002 Granada, Spain

ARTICLE INFO

*Keywords:*
Authigenic
Environmental conditions
Illitization
Illite-smectite mixed-layers
Palygorskite
X-ray diffraction

ABSTRACT

This study presents a mineralogical analysis of the effect of hypersaline lake environments rich in organic matter on the mineral transformations in sediments of the eastern part of the Guadix-Baza Basin (Betic Cordillera). Dark sediments with fragments of organic matter are rich in phyllosilicates (K-white mica, illite-smectite mixed layers, –I/S– minor amounts of paragonite, palygorskite, chlorite and kaolinite) and contain quartz, feldspars, and framboidal pyrite. X-ray diffraction patterns of I/S (R0 type, disordered) revealed a continuous between the positions of pure smectite and 30% of illite layers. Chemical composition of I/S mixed layers indicated a significant beidellitic substitution of Si by $Al^{IV}$, Fe + Mg > 1 atoms per formula unit (a.p.f.u.) and K content up to 0.42 a.p.f.u. These data suggested the presence of a minor and variable amount of illitic layers among the major smectitic ones. Saline waters of the lake and the reducing environment of the sediment favored Mg and $Fe^{2+}$ uptake, generating octahedral negative charge, which together with the beidellitic substitution would provide clay layer negative charge enough to admit K incorporation in the interlayer, hence the beginning of a diagenetic low temperature illitization.

## 1. Introduction

Clay mineral composition of lake sediments is the result of detrital and authigenic processes in the deposit basin due to fluctuations of environmental conditions. Wet periods can produce an increase of detrital inputs by strong rain events and a high influx of weathered silicates. Dry periods can promote lake water evaporation that in closed paleolakes produces alkalinity and salinity increasing that favors authigenic clay mineral neoformation. Deocampo et al. (2017) suggested that Al-rich muds accumulated during humid times and Mg-rich muds accumulated during arid times in eastern African lakes. The extreme conditions produced in the hydrologically restricted environments of paleolakes (salinity, Eh, pH, microbiological activity) can act as catalysts for the processes of neoformation and transformation of minerals in sediments. In these settings, detrital clays can interact with saline fluids, leading to mineral transformations. Even fast reactions can play an important role in the uptake of elements (such as K, Mg or Fe) (Cuadros et al., 2017) considering that clay minerals provide important reactive surfaces for adsorption and desorption of elements and compounds that can be incorporated into the new clay phases. These reactions are favored in systems where the chemistry of reacting fluids is very far from equilibrium with clay minerals (Drief et al., 2002). In sedimentary environments, high concentration of waters and low rates of organic matter decay in reducing conditions that favors microbial redox reactions involving Fe and S compounds are important factors that control sequential mineral transformations of clays (Noël et al., 2017; Kasina et al., 2017; Andrade et al., 2018). Specifically, as clays alter in saline water, octahedral cation changes can increase layer charge, and smectite can convert to illite (Deocampo, 2015). Low-temperature illitization can occur through repeated desiccation cycles or through interaction with K-rich brines (Deocampo et al., 2009). This paper addresses the effect of extreme physical and chemical conditions of hypersaline lake environments rich in organic matter on the mineral transformations in sediments of the eastern part of the Guadix-Baza Basin. Furthermore, this study could be an interesting tool for identifying and recognizing these kinds of environments during the Quaternary, which help to understand important processes in current worldwide basins in relation to global change.

## 2. Geological context

The study area is located in the eastern part of the Guadix-Baza

* Corresponding author.
*E-mail address:* jmillan@ujaen.es (J. Jiménez-Millán).

https://doi.org/10.1016/j.clay.2020.105739
Received 13 December 2019; Received in revised form 11 June 2020; Accepted 13 June 2020

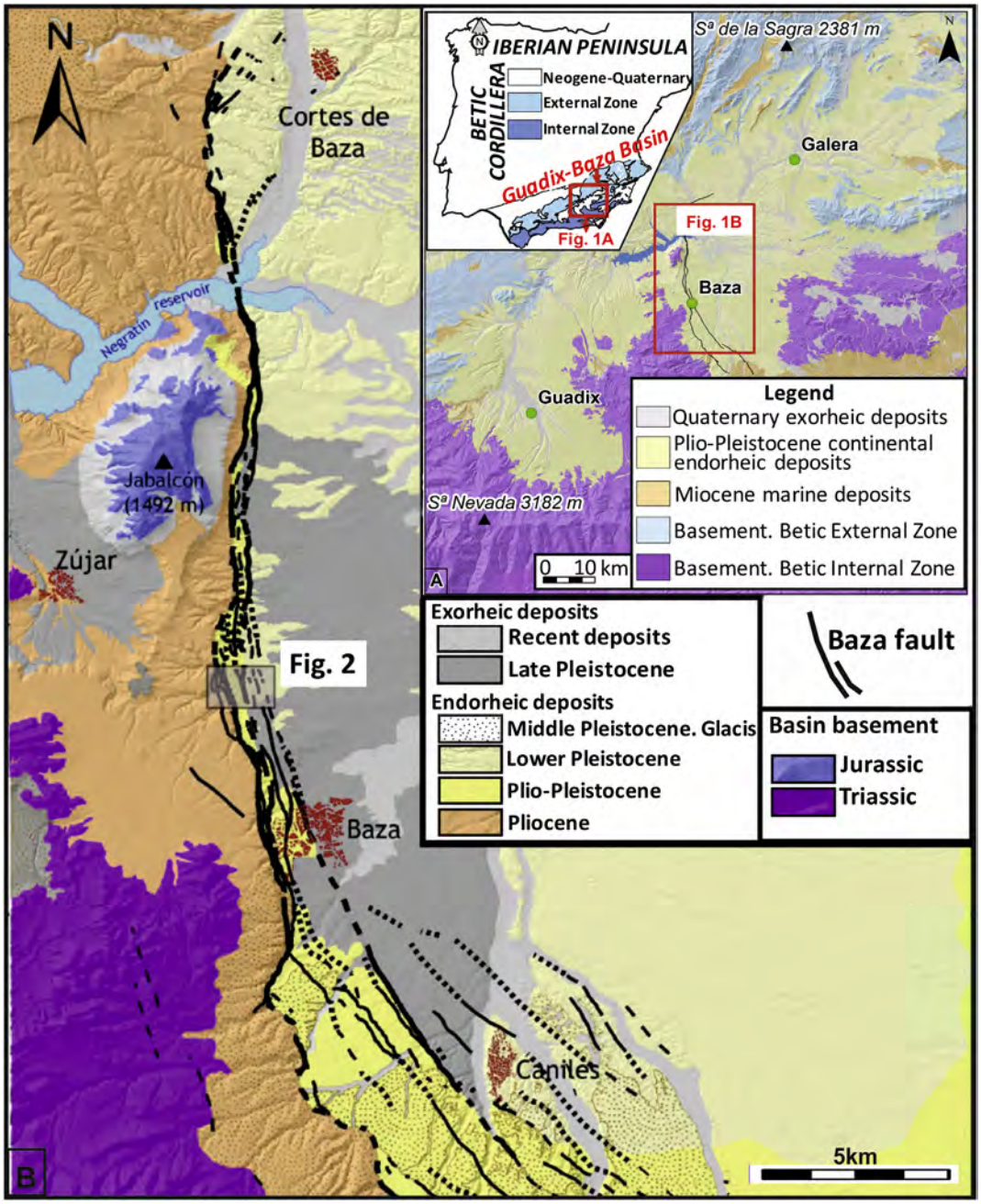


**Fig. 1.** A) Geographical and geological location maps of the Betic Cordillera and the Guadix-Baza Basin. B) Local map of the Baza Fault area. The squared area shows the location of the study sector within the Baza Fault represented in Fig. 2 (online version in color).

Basin, the largest Neogene intramontane basin in the eastern Betic Cordillera (SE Spain) (Fig. 1A).

The sedimentological and geomorphological evolution of the basin has been influenced by the Baza Fault, a major tectonic structure of the Guadix-Baza Basin (Fig. 1b). The basin presents a highly asymmetric structure, with sediment thickness increasing westward, up to a maximum observed thickness of ca. 2200 m near the Baza Fault (Haberland et al., 2017). The sedimentary fill of this basin consists of upper Miocene marine rocks and Pliocene/Pleistocene fluvial and lacustrine rocks (Fig. 1b) (Vera, 1970). The marine to continental transition was the consequence of regional uplift of the Betic Cordillera. The relief generation produced an endorheic intra-mountain depression allowing endorheic continental sedimentation in the basin during the Pliocene and most of the Pleistocene. The presence of the Baza Fault made possible the subsidence in the eastern sector in relation to the western one, generating significant accumulations of evaporitic sediments in that sector with especially saline periods in the waters of the basin (Vera, 1970; García-Tortosa et al., 2008, 2011; Gibert et al., 2007). The stratigraphic study and facies mapping of Gibert et al. (2007) showed three gradational lithological zones (inner, intermediate and marginal). The studied samples in the present paper belong to the "Benamaurel Unit", a term used to designate the sedimentary deposits of the inner and the intermediate lithologic zones of the basin, comprising subhorizontal lacustrine deposits rich in carbonate, marls, gypsum and dark claystones bearing native sulphur nodules. Extensive sedimentation in the Guadix-Baza Basin ended when the basin became exorheic in the middle Pleistocene (ca. 500 ka), after a tributary of the Guadalquivir river captured the basin and generated the present drainage system.

The studied rocks outcrop along the central segment of the Baza

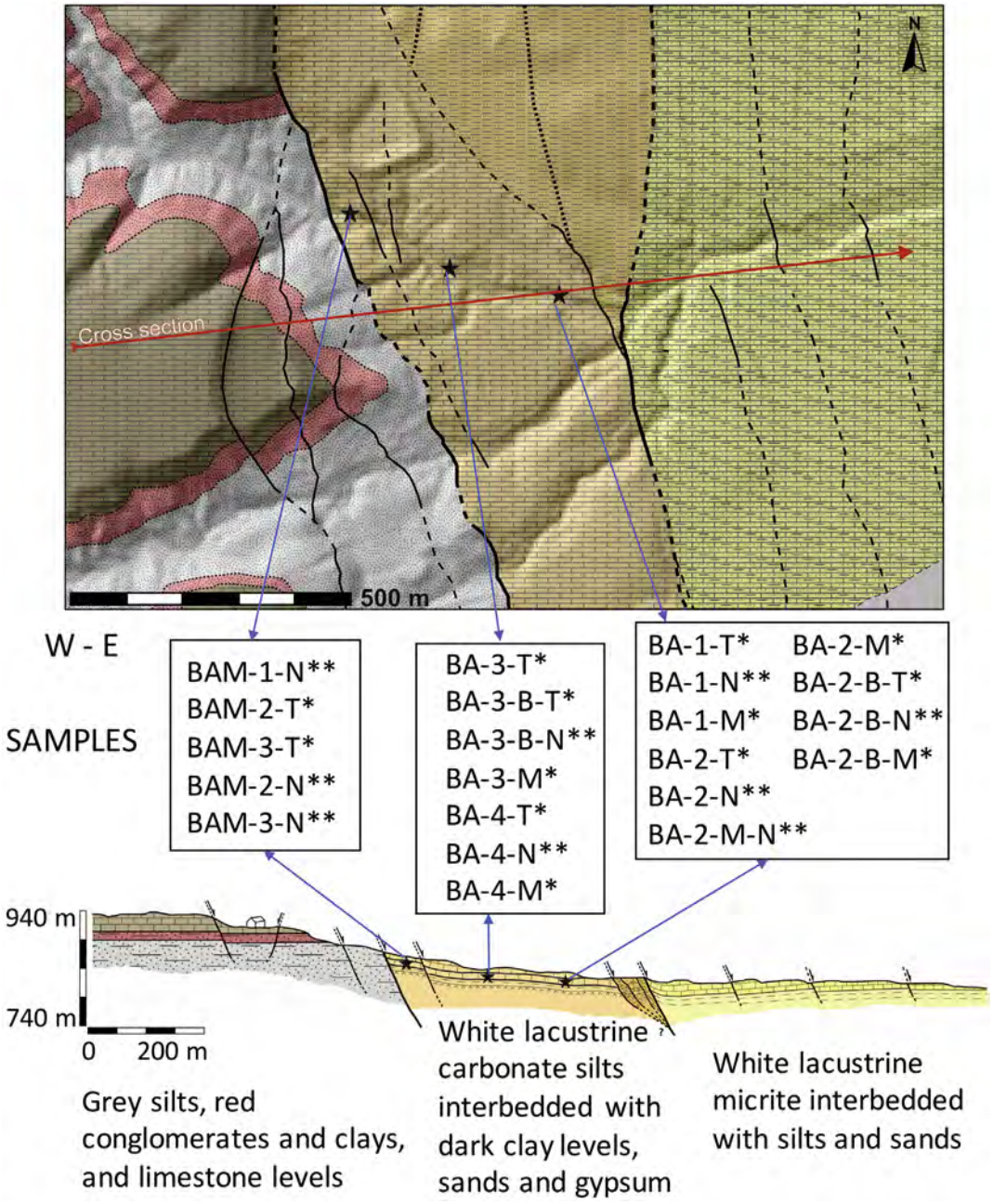


**Fig. 2.** Local geology map of the Baza Fault area. Red line shows the cross section represented in the bottom of the figure. Black stars mark the location of the studied samples. * Carbonate-rich layers; ** Dark clay-rich layers (online version in color).
(For interpretation of the references to color in this figure legend, the reader is referred to the web version of this article.)

Fault (Barranco del Agua site), including Plio/Pleistocene soft rocks from the intermediate zone of the Benamaurel Unit (Fig. 2). The studied outcrops are located between two main strands of the Baza Fault. White lacustrine carbonate beds up to 50 cm thick appear intercalated with thin grey lutite and silt layers. These lithofacies are very rich in carbonates, with dolomite predominating over calcite; the amount of quartz, feldspars, phyllosilicates and gypsum is very low. Dark, almost black sediments from a few millimeters to several decimeters thick made of clays and silts with abundant organic matter are intercalated in the stratigraphic sequence of the sector. Their ages vary between 3 million years and 1 million years (García-Tortosa et al., 2011). A set of 22 samples were analyzed (location is indicated in Fig. 2) of which three black levels in the footwall fault block and five levels in the hanging wall block were identified and studied.

## 3. Methods

The X-ray-diffraction (XRD) data of the sediments were obtained from powders and oriented aggregates (whole sample and < 2 μm fraction), after washing with pure and ultrapure water to remove salts. Oriented aggregates were prepared by settling a dispersion in a glass holder. The < 2 μm fraction were separated by centrifugation. Ethylene glycol treatment was carried out to assist in the identification of expandable minerals (smectite, interstratified layers, etc.). The diffractograms were obtained in two PANalytical X'Pert Pro diffractometers (CuKα radiation, 45 kV, 40 mA) equipped with an X'Celerator solid-state linear detector, using a step increment of 0.008° 2θ and a total counting time of 10 s/step. A sweep between 3° and 62° 2θ was done on the dry samples, while for the glycolated samples the sweep was between 2° and 30° 2θ in order to confirm the identification of expandable

minerals. We applied decomposition routines included in the HighScore software. Peaks were fitted through a Voigt function (mixed Gaussian and Lorentzian). Various combinations of peaks were proven until we acquired the lowest residuum. Intensity, half-height width and peak position were approximated by the least-squares method until they optimally retraced the peak course of the original profile.

Textural and chemical observations in a scanning electron microscope (SEM) were made on polished sections using back-scattered electrons (BSE) in atomic number contrast mode, and on rock fragments in secondary electron mode (SE). BSE images were acquired at 15 kV with a working distance of 8 mm using an AsB detector, whereas SE images were acquired at 15 kV using conventional and In-Lens detectors in a Merlin Carl Zeiss electron microscope.

For the textural and chemical characterization at the nanometer scale, selected samples according to XRD analysis and SEM observations were prepared for transmission electron microscopy (TEM) study. Samples were prepared using Au and Cu grid surface coated in a perforated formvar resin from a dispersion of finely ground sample particles, in alcohol or distilled water. The monomineralic character of each grain is proven by its electron diffraction pattern, checking the existence of a single network and, therefore, a single crystalline phase. The TEM data was obtained using two electron microscopes: the HAADF FEI TITAN G2 microscope, operated at 300 kV, and the Philips CM20 (STEM) microscope, operated at 200 kV. Quantitative analyses (AEM) of particles were obtained in STEM mode with an EDAX microanalysis system in a Philips CM20 and a HAADF FEI TITAN G2 electron microscopes. The counting time used was 100 s except for Na and K, which were analyzed for 15 s to try to minimize alkali-loss problems as short counting times improve reproducibility for K and Na (Nieto et al., 1996). Albite, biotite, spessartine, muscovite, olivine, titanite, MnS and CaS were used as standards to derive k- factors for the transformation of intensity ratios to concentration ratios following the procedures of Cliff and Lorimer (1975).

The total organic carbon (TOC) of the sediments was determined by indirect measurement on an automatic total organic carbon analyzer (Shimadzu TOC-VCSH), obtained by the difference between total carbon (TC) and total inorganic carbon (TIC).

## 4. Mineral assemblage

X-ray diffraction analyses revealed that lacustrine carbonate sediments are rich in dolomite (Fig. 3A) and have a low content of quartz, calcite, feldspars and phyllosilicates. Oriented aggregates patterns of whole samples and the < 2 μm fraction showed the presence of muscovite, paragonite, kaolinite and a small amount of smectite in the clay assemblage (Fig. 3B). Nevertheless, dark levels are rich in phyllosilicates, quartz and feldspars (Fig. 4A). Oriented aggregates patterns of whole samples and the < 2 μm fraction showed that the clay assemblage is dominated by K-white mica, illite-smectite mixed layers (I/S) and minor amounts of paragonite, chlorite and kaolinite (Fig. 4B and 5). Ethylene glycol treatment revealed the presence of chlorite, which had been hidden by the (001) reflection of I/S. A paragonite peak, partially overimposed on the (002) reflection of muscovite, was also recognized. The study of the reflections around 0.7 nm and 0.35 nm revealed the (001)/(002) reflections of kaolinite as well as the (002)/(004) reflections of chlorite.

Broad $d_{001}$ peaks between 1.4 and 1.5 nm shifted around 1.7 nm after ethylene glycol treatment. Moreover, small reflections after ethylene glycol around 9°2θ (002) and 16°2θ (003) indicated the presence of an illite-smectite (R0 type, disordered) mixed-layer, constituted mainly by smectite layers. These small reflections were recognized when the air-dried (AD) and ethylene glycol (EGC) treated diagrams of the same specimen were superposed (Fig. 5); the areas in which the EGC diagram separates from - and shows a higher intensity than - the AD one corresponds to swelling material (smectite and/or I/S). These areas in the distinctive regions of the percentage of illitic

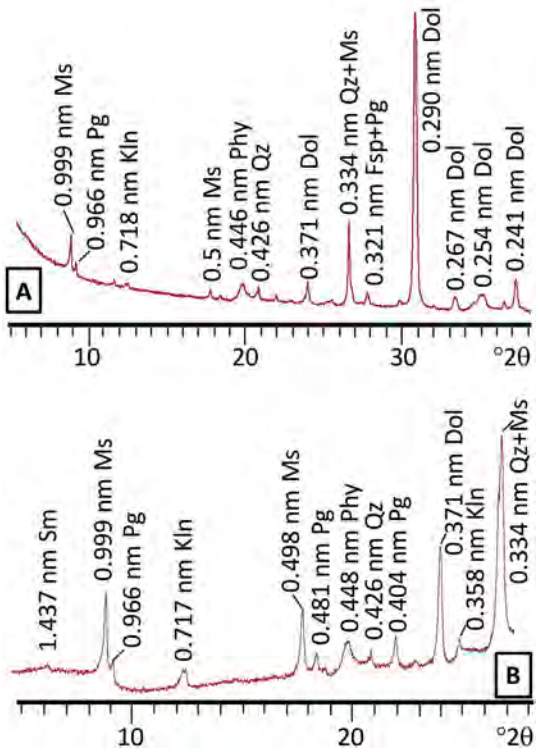


**Fig. 3.** XRD patterns of carbonate-rich layers of the sequence (A) Representative bulk disoriented powder pattern. (B) Representative diffractogram of oriented aggregate (< 2 μm sample). Dol: dolomite, Sm: smectite, Kln: kaolinite, Ms.: muscovite, Pg: paragonite, Qz: quartz. Fsp: feldspar.

layers (according to Moore and Reynolds, 1997) are more a continuous than a single peak. In Fig. 5 we have indicated the theoretical position of a pure smectite and of an I/S having 30% illitic layers. The bands corresponding to the index reflections cover all the range of Δ°2θ between these extremes, which indicated that the proportion of illite layers in the R0 I/S oscillates between 0 and, at least, 30%. Similar behavior of I/S is recognized in the sediments of the hanging-wall and footwall fault blocks.

From a textural point of view, SEM images of the dark sediments showed that the I/S crystals are small (< 5 μm) and form the matrix of the rock (Fig. 6A). They have smectitic compositions and identified as smectite rich I/S, according to XRD results (see above). Some small crystals of mica appear in the microlamination of the sediment. Detrital fragments of micas and chlorites are mostly present in the coarse size fraction, 50 μm on average (Fig. 6B). Kaolinite aggregates (Fig. 7A), plant fragments (Fig. 7B) and pyrite framboids partially oxidized to hematite (Fig. 7A and C) are also abundant. The presence of small prismatic crystals of palygorskite smaller than 1 μm was detected in the TEM images (Fig. 8A). HRTEM images show flakes of I/S poorly crystalline aspect where scarce layers collapsed to 10 Å can be identified (Fig. 8B).

The AEM microanalyses (Table 1, Fig. 9) of the I/S mixed layers in the dark sediments are characterized by the incorporation of octahedral Fe and Mg (Fe + Mg > 1, a.p.f.u. normalized to 11 oxygens). Moreover, K content in the interlayer can reach up to 0.42 a.p.f.u. Octahedral sums are in some analyses significantly higher than 2.0. This characteristic, together with interlayer charge slightly small and a high overall content in Mg, could indicate that a part of Mg may be in the interlayer, instead of the octahedral position (Sánchez Roa et al., 2018). Nevertheless, we have not tried a distribution of this element between the two possible layers, due to lack of objective criteria to do it. Therefore, its assignation to the octahedral layer in Table 1 must be considered only for presentation purpose, which implies that the real

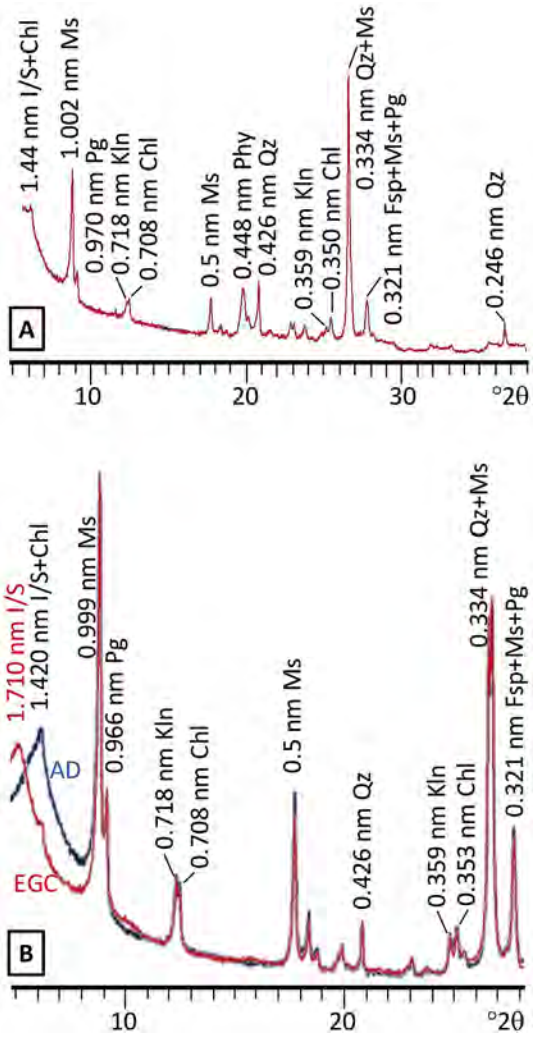


**Fig. 4.** XRD patterns of the dark clay-rich layers of the sequence (A) Representative bulk disoriented powder pattern. (B) Representative diffractogram of oriented aggregate (whole sample). AD: air dried (in blue), and EGC: treated with ethylene-glycol (in red). Chl: chlorite, Kln: kaolinite, Ms.: muscovite, Pg: paragonite, Qz: quartz. Fsp: feldspar. I/S: illite-smectite mixed layers. (For interpretation of the references to color in this figure legend, the reader is referred to the web version of this article.)

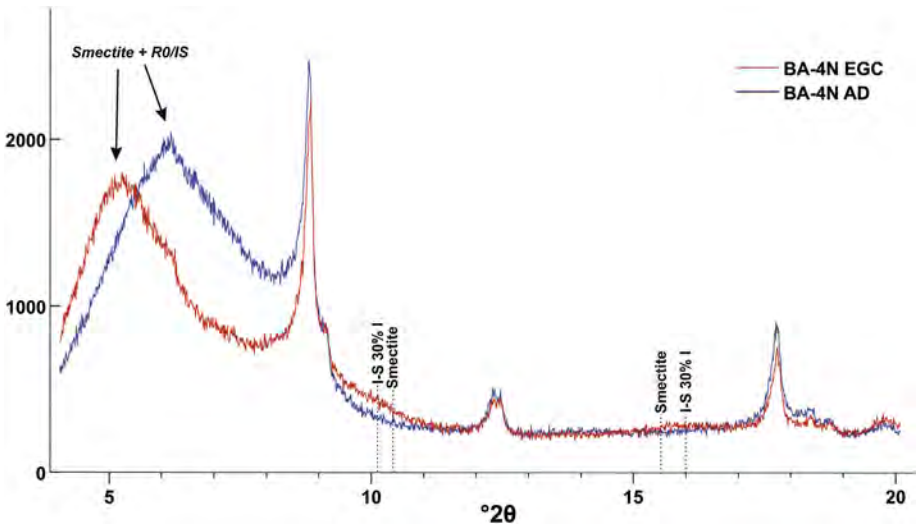


**Fig. 5.** Representative diffractogram of oriented aggregate (< 2 μm sample) from dark sediments, including the theoretical position of a pure smectite and of an I/S having 30% illitic layers. AD: air dried (in blue), and EGC: treated with ethylene-glycol (in red). (For interpretation of the references to color in this figure legend, the reader is referred to the web version of this article.)

octahedral sums are lower and interlayer charges are higher than those presented in the table. Taking into account these considerations, the compositions presented in Table 1 are perfectly coherent with smectite or smectite-rich I/S, having a major beidellitic component. Palygorskite composition has significant amounts of Fe (Table 1). This composition is within the range compiled from the literature by García-Romero and Suárez (2010) and, according to these authors, within the polysomatic series between this mineral and sepiolite it corresponds to an ideal palygorskite. The composition of the detrital micas and chlorites are coherent with metamorphic-origin compositions and similar to other detrital phyllosilicates reported in sediments from the Guadix-Baza Basin (Sánchez Roa et al., 2017; 2018).

Smectite from the carbonate layers have an Al-rich dioctahedral compositions, with low Fe, Mg and K contents (Table 1, Fig. 9).

TOC contents of the sediments range from 1.53 to 0.02 wt% (Table 2). Original values were probably higher since it is known that recent weathering contributes to the TOC loss due to the infiltration of $O_2$-rich meteoric water (Suan et al., 2013). Organic carbon ratio (Organic Carbon/Total Carbon, OCR) is very low in the carbonate-rich sediments (< 0.15). Dark clay rich-layers have higher OCR values (Table 2, up to 1).

## 5. Discussion

Textural and mineral composition data of the mineral assemblages of the study area suggested important differences in the effect of carbonate precipitation and the influx of detrital material on the sediments of the sequence. Thick carbonate-rich layers were clay mineral-poor suggesting low detrital contribution and fast carbonate precipitation (see Gibert et al., 2007). The presence of smectite was restricted to the dolomite-rich sediments with low organic carbon ratio (OCR) (Table 2). Samples with higher OCR were characterized by the presence of I/S. Fast dolomite precipitation involved in the formation of the carbonate-rich layer produced a sealing effect favoring the organic carbon dilution in the sediments and limiting the extent of the reduction process due to the organic matter decay. Moreover, dolomite precipitation acted as a sink for Mg and diminished sediment permeability, decreasing the interaction of the detrital smectite with fluid-pores and avoiding the progress of the illitization process. On the other hand, sediments enriched in phyllosilicates and plant residues within the carbonate lake sequence suggested the existence of stages of high detrital contribution. The presence of large and fractured crystals of chlorite and mica pointed to a detrital origin for these phyllosilicates. In addition, the presence of these mineral phases as well as paragonite clearly indicated a source for these sediments that lies, in the basement rocks of the

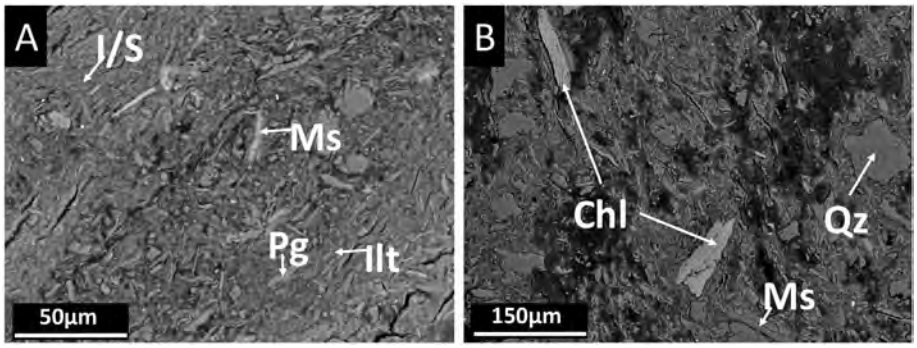


**Fig. 6.** BSE images showing the general aspect of the black sediments: (A) detail of the matrix with the common presence of smectite rich I/S grains next to fine-grained dioctahedral micas (muscovites and paragonites); (B) aspect of the coarse fraction composed of detrital grains of phyllosilicates (muscovite and chlorite) and quartz. I/S: illite-smectite mixed-layers, Ms.: muscovite, Pg: paragonite, Qz: quartz.

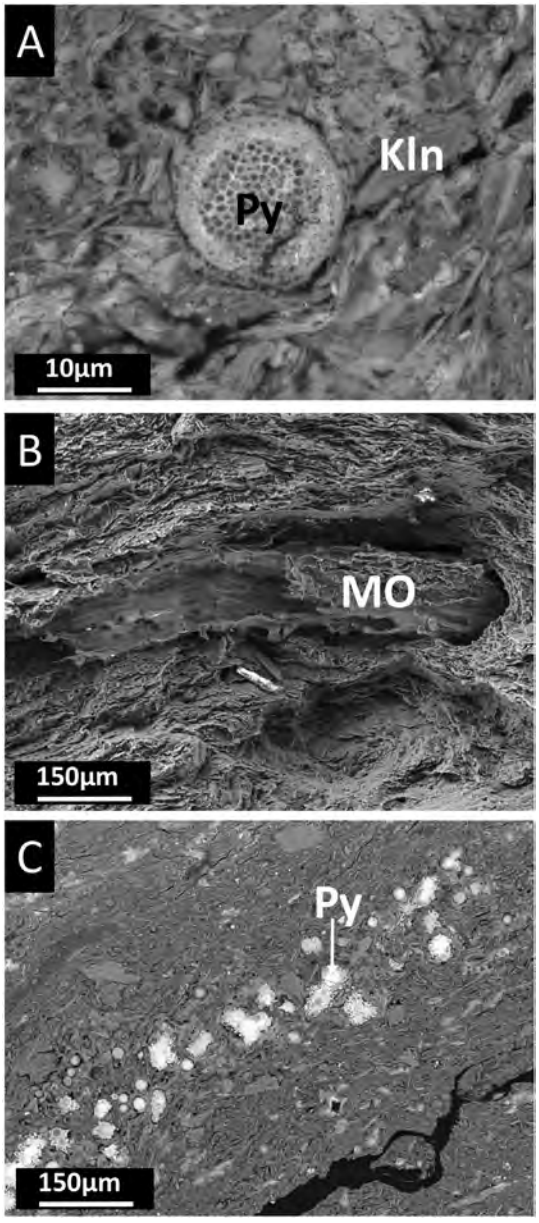


**Fig. 7.** SEM images corresponding to kaolinite aggregates also common in these sediments and a well-developed pyrite framboid (A), organic matter remains (plant fragments) (B) and a rich-level in pyrite framboids showing a lighter color as a consequence of a partial oxidation to hematite (C). Kln: kaolinite, OM: organic matter, Py: pyrite.

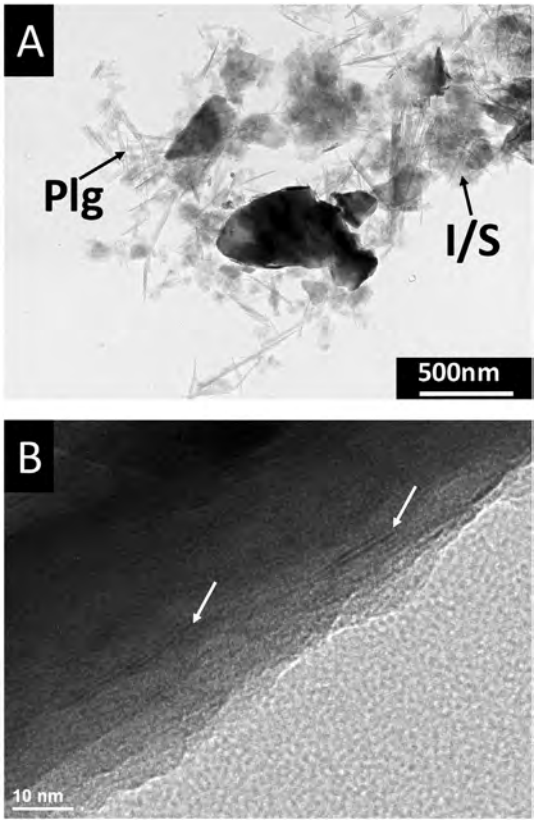


**Fig. 8.** TEM images: (A) prismatic crystals of palygorskite (< 1 µm) and illite-smectite grains; (B) high resolution image of very poor crystalline flakes with some layers collapsed to 10 Å (white arrows). Lattice fringes were observed on the edge of a sheet folded up to vertical position. I/S: illite-smectite mixed-layers, Plg: palygorskite.

Internal Zone of Betic Cordillera, of metamorphic origin. Specifically, the metamorphic rocks of the Alpujarride and Nevado-Filabride metamorphic complexes of the inner part of the Betic Cordillera were considered as the most likely source of the primary minerals. Chlorite and mica were also recognized as detrital minerals in the marginal area of the Baza sub-basin (Galera Gypsum Unit) by Sánchez-Roa et al. (2016). Detrital micas and chlorites, together with feldspars, are frequently altered to kaolinite and/or smectite; kaolinite aggregates can also be observed as the result of intense silicate hydrolysis during wet conditions. Naturally, wet climate will favor an increase in weathering, erosion and transport, explaining the influx of detrital and progressively weathered silicates. Therefore, micas, chlorites and kaolinite assemblages suggested periods of freshwater supply to the lake, probably related to wetter climatic events (Foester et al., 2018), which allowed the weathering and erosion of the Internal Zone of the Betic Cordillera surrounding reliefs.

**Table 1**
Structural formulae calculated from AEM data. Micas and smectites normalized to $O_{10}(OH)_2$. $^{IV}Al = (4 - Si)$. Chlorite normalized to $O_{10}(OH)_8$. Palygorskite normalized to $O_{20}(OH)_2$. O.C.: octahedral charge for I/S and smectite.

| | Si | $Al^{IV}$ | $Al^{VI}$ | Fe | Mg | Mn | Ti | $\Sigma^{VI}$ | O.C. | Ca | K | Na | $\Sigma^{XII}$ |
|---|---|---|---|---|---|---|---|---|---|---|---|---|---|
| a. Illite-smectite mixed layers | | | | | | | | | | | | | |
| BA3N-4 | 3.65 | 0.35 | 1.04 | 0.58 | 0.54 | 0.00 | 0.00 | 2.16 | −0.06 | 0.01 | 0.42 | 0.00 | 0.43 |
| BA3N-7 | 3.72 | 0.28 | 1.65 | 0.32 | 0.10 | 0.00 | 0.00 | 2.07 | 0.11 | 0.05 | 0.08 | 0.03 | 0.16 |
| BA3N-8 | 3.81 | 0.19 | 1.52 | 0.28 | 0.29 | 0.00 | 0.00 | 2.09 | −0.02 | 0.05 | 0.10 | 0.02 | 0.17 |
| BA3N-11 | 3.60 | 0.40 | 1.27 | 0.49 | 0.38 | 0.00 | 0.00 | 2.14 | 0.04 | 0.06 | 0.21 | 0.02 | 0.29 |
| BA4N-1 | 3.68 | 0.32 | 1.62 | 0.35 | 0.11 | 0.00 | 0.00 | 2.08 | 0.13 | 0.05 | 0.09 | 0.03 | 0.17 |
| BA4N-5 | 3.63 | 0.37 | 1.29 | 0.47 | 0.37 | 0.00 | 0.00 | 2.13 | 0.02 | 0.06 | 0.19 | 0.03 | 0.28 |
| BA4N-9 | 3.70 | 0.30 | 1.06 | 0.57 | 0.52 | 0.00 | 0.00 | 2.15 | −0.07 | 0.03 | 0.31 | 0.02 | 0.36 |
| BAM3N-2 | 3.78 | 0.22 | 1.09 | 0.53 | 0.49 | 0.00 | 0.00 | 2.11 | −0.16 | 0.02 | 0.34 | 0.01 | 0.37 |
| BAM3N-3 | 3.69 | 0.31 | 1.08 | 0.52 | 0.55 | 0.00 | 0.00 | 2.15 | −0.10 | 0.03 | 0.36 | 0.01 | 0.40 |
| BAM4N-7 | 3.72 | 0.28 | 1.17 | 0.48 | 0.50 | 0.00 | 0.00 | 2.15 | −0.05 | 0.02 | 0.30 | 0.01 | 0.33 |
| BA2N-2 | 3.75 | 0.25 | 1.06 | 0.52 | 0.57 | 0.00 | 0.00 | 2.15 | −0.12 | 0.04 | 0.39 | 0.03 | 0.46 |
| BA2N-5 | 3.58 | 0.42 | 1.24 | 0.52 | 0.37 | 0.00 | 0.00 | 2.13 | 0.02 | 0.04 | 0.26 | 0.01 | 0.31 |
| BA2N-6 | 3.66 | 0.34 | 1.64 | 0.33 | 0.10 | 0.00 | 0.00 | 2.07 | 0.11 | 0.03 | 0.09 | 0.03 | 0.15 |
| BA2N-9 | 3.74 | 0.26 | 1.15 | 0.48 | 0.52 | 0.00 | 0.00 | 2.15 | −0.07 | 0.02 | 0.35 | 0.01 | 0.38 |
| BA2N-13 | 3.80 | 0.20 | 1.79 | 0.14 | 0.10 | 0.00 | 0.00 | 2.03 | −0.01 | 0.06 | 0.11 | 0.01 | 0.18 |
| BAM1N-1 | 3.64 | 0.36 | 1.07 | 0.57 | 0.54 | 0.00 | 0.00 | 2.18 | 0.00 | 0.01 | 0.36 | 0.00 | 0.37 |
| BAM1N-7 | 3.83 | 0.17 | 1.55 | 0.25 | 0.31 | 0.00 | 0.00 | 2.11 | 0.02 | 0.04 | 0.10 | 0.02 | 0.16 |
| BAM1N-8 | 3.67 | 0.33 | 1.82 | 0.12 | 0.11 | 0.00 | 0.00 | 2.05 | 0.04 | 0.07 | 0.11 | 0.03 | 0.21 |
| BAM1N-11 | 3.62 | 0.38 | 1.23 | 0.50 | 0.41 | 0.00 | 0.00 | 2.14 | 0.01 | 0.04 | 0.31 | 0.01 | 0.36 |
| b. Smectite | | | | | | | | | | | | | |
| BA4T-3 | 3.68 | 0.32 | 1.85 | 0.09 | 0.12 | 0.00 | 0.00 | 2.06 | 0.06 | 0.06 | 0.06 | 0.02 | 0.14 |
| BA4T-6 | 3.73 | 0.27 | 1.79 | 0.12 | 0.14 | 0.00 | 0.00 | 2.05 | 0.01 | 0.07 | 0.09 | 0.01 | 0.17 |
| BA4T-7 | 3.65 | 0.35 | 1.88 | 0.07 | 0.09 | 0.00 | 0.00 | 2.04 | 0.03 | 0.07 | 0.09 | 0.02 | 0.18 |
| BA4T-9 | 3.75 | 0.25 | 1.81 | 0.11 | 0.15 | 0.00 | 0.00 | 2.07 | 0.06 | 0.05 | 0.10 | 0.02 | 0.17 |
| BA4T-12 | 3.81 | 0.19 | 1.84 | 0.09 | 0.11 | 0.00 | 0.00 | 2.04 | 0.01 | 0.05 | 0.10 | 0.01 | 0.16 |
| BA2M-1 | 3.78 | 0.22 | 1.87 | 0.08 | 0.10 | 0.00 | 0.00 | 2.05 | 0.05 | 0.03 | 0.09 | 0.02 | 0.14 |
| | 3.79 | 0.21 | 1.84 | 0.08 | 0.13 | 0.00 | 0.00 | 2.05 | 0.02 | 0.03 | 0.09 | 0.02 | 0.14 |
| BA2M-2 | 3.80 | 0.20 | 1.79 | 0.14 | 0.11 | 0.00 | 0.00 | 2.04 | 0.01 | 0.06 | 0.11 | 0.01 | 0.18 |
| BA2M-5 | 3.66 | 0.34 | 1.83 | 0.13 | 0.09 | 0.00 | 0.00 | 2.05 | 0.06 | 0.07 | 0.10 | 0.03 | 0.20 |
| BA2M-6 | 3.82 | 0.18 | 1.86 | 0.08 | 0.11 | 0.00 | 0.00 | 2.05 | 0.04 | 0.03 | 0.08 | 0.02 | 0.13 |
| BA2M-9 | 3.68 | 0.32 | 1.85 | 0.09 | 0.12 | 0.00 | 0.00 | 2.06 | 0.06 | 0.06 | 0.06 | 0.02 | 0.14 |
| b. Palygorskite | | | | | | | | | | | | | |
| BA3N-5 | 7.82 | 0.18 | 1.71 | 0.39 | 1.88 | 0.00 | 0.00 | 3.98 | – | 0.00 | 0.00 | 0.00 | 0.00 |
| BA3N-6 | 7.78 | 0.22 | 1.62 | 0.46 | 1.96 | 0.00 | 0.00 | 4.04 | – | 0.00 | 0.00 | 0.00 | 0.00 |
| BA4N-6 | 7.81 | 0.19 | 1.73 | 0.36 | 1.91 | 0.00 | 0.00 | 4.00 | – | 0.00 | 0.00 | 0.00 | 0.00 |
| BAM3N-5 | 7.83 | 0.17 | 1.73 | 0.35 | 1.89 | 0.00 | 0.00 | 3.97 | – | 0.00 | 0.00 | 0.00 | 0.00 |
| c. Micas | | | | | | | | | | | | | |
| BA3N-12 | 3.16 | 0.84 | 1.71 | 0.18 | 0.11 | 0.02 | 0.00 | 2.02 | – | 0.01 | 0.89 | 0.06 | 0.96 |
| BA3N-14 | 3.14 | 0.86 | 1.76 | 0.15 | 0.10 | 0.00 | 0.00 | 2.01 | – | 0.01 | 0.90 | 0.03 | 0.94 |
| BA3M-8 | 3.24 | 0.76 | 1.72 | 0.12 | 0.16 | 0.00 | 0.00 | 2.00 | – | 0.01 | 0.02 | 0.89 | 0.92 |
| BAM4N-9 | 3.28 | 0.72 | 1.69 | 0.20 | 0.11 | 0.00 | 0.00 | 2.00 | – | 0.01 | 0.02 | 0.82 | 0.85 |
| d. Kaolinite | | | | | | | | | | | | | |
| BA4N-9 | 4.02 | 0.00 | 3.88 | 0.09 | 0.00 | 0.01 | 0.00 | 3.98 | – | – | – | – | – |
| BAM3N-7 | 4.01 | 0.00 | 3.91 | 0.07 | 0.01 | 0.01 | 0.00 | 4.00 | – | – | – | – | – |
| e. Chlorite | | | | | | | | | | | | | |
| BA3N-10 | 2.65 | 1.35 | 1.33 | 2.98 | 1.68 | 0.01 | 0.01 | 6.00 | – | – | – | – | – |
| BAM3N-11 | 2.68 | 1.32 | 1.42 | 3.04 | 1.48 | 0.05 | 0.03 | 5.99 | – | – | – | – | – |

On the other hand, sediments with high OCR are characterized by the presence of pyrite framboids, an illite/smectite phase enriched in Fe, Mg and K and palygorskite (Table 2). This could suggest processes of authigenic crystallization during or after deposition, which had an important impact on the composition of the sedimentary record. The crystallization of individual pyrite crystals in framboidal pyrite are often associated with organic matter (Love, 1967; Love et al., 1984; Folk, 2005). Pyrite frequently appears in the interstices of the carbonaceous material structure (MacLean et al., 2007; Maclean et al., 2008), suggesting that the buried organic matter can promote microbial sulfate reduction and the production of pyrite. For example, nanobacterial cells have been frequently found coating pyrite microcrystals associated with decaying organic matter (Folk, 2005). In the black sediments from Baza, the presence of pyrite framboids is associated to fragments of organic matter (Fig. 7).

In a hydrological restricted environment, such as that of the lake in the eastern part of the Guadix-Baza Basin, hypersaline evaporitic brines with a high Mg/Ca ratio were developed (Gibert et al., 2007). The hydrochemistry of lake- and porewaters frequently respond to fluctuations in the precipitation/evaporation ratio (Deocampo, 2004; Deocampo et al., 2017), which control the formation and composition of authigenic clay minerals. When Mg/Ca ratios rise in the residual waters, Mg silicates can precipitate from Mg-rich fluids (Deocampo, 2015). The presence of small palygorskite authigenic crystals in the black sediments from the lake sector of Baza was used as an indicator of the Mg enrichment process of the fluid. Palygorskite crystallization is associated with arid climates and evaporites (e.g., Millot, 1964; Post, 1978; Weaver and Beck, 1977), which is consistent with both the existence of saline waters and the progressive increasing towards conditions of greater aridity (Hugget et al., 2016). The control of salinity in closed basins has been described for numerous lakes (Singer and Stoffers, 1980; Hay et al., 1991; Renaut, 1993; Deocampo and Renaut, 2016). Foester et al. (2018) indicated that the control of salinity in these contexts depends on fluctuations in the moisture influx, which, in

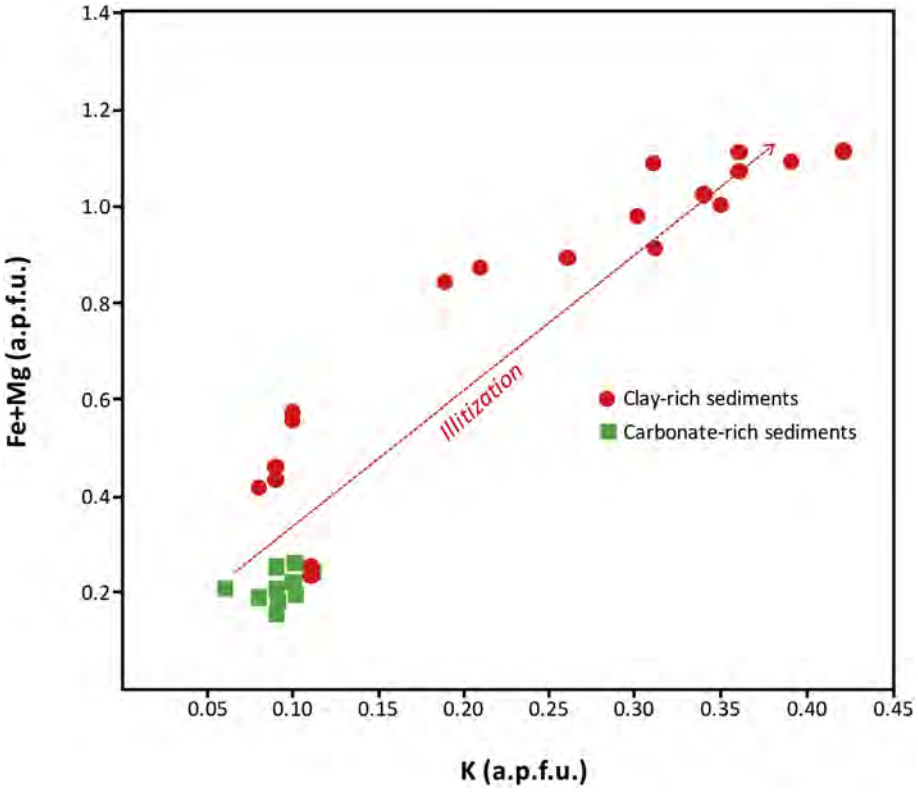


**Fig. 9.** Plots of AEM analyses of smectite and R0 I/S mixed layers (on line version is in color).

**Table 2**
Carbon content and mineral assemblages of the sediments.

| Sample | TC (%) | IC (%) | TOC (%) | OCR | I/S | Sm | Plg | Py | Qz | Ms | Pg | Chl | Cal | Dol |
|---|---|---|---|---|---|---|---|---|---|---|---|---|---|---|
| BA-1-T* | 6.70 | 6.31 | 0.40 | 0.06 | – | x | – | – | x | x | x | – | x | xxx |
| **BA-1-N**** | **0.94** | **0.80** | **0.14** | **0.15** | **xx** | **–** | **–** | **x** | **xxx** | **xxx** | **x** | **x** | **x** | **–** |
| BA-1-M* | 12.13 | 10.60 | 1.53 | 0.13 | – | x | – | – | x | x | x | – | x | xxx |
| BA-2-T* | 11.53 | 10.00 | 1.53 | 0.13 | xx | – | – | – | x | x | x | – | x | xxx |
| **BA-2-N**** | **0.06** | **< 0.10** | **0.06** | **1.00** | **xx** | **–** | **x** | **x** | **xxx** | **xxx** | **x** | **x** | **x** | **–** |
| **BA-2-M-N**** | **4.09** | **3.63** | **0.56** | **0.14** | **xx** | **–** | **–** | **x** | **xxx** | **xxx** | **x** | **x** | **x** | **–** |
| BA-2-M* | 9.72 | 8.61 | 1.11 | 0.11 | – | x | – | – | x | x | x | – | x | xxx |
| BA-2-B-T* | 12.73 | 11.96 | 0.77 | 0.06 | – | x | – | – | x | x | x | – | x | xxx |
| **BA-2-B-N**** | **1.04** | **0.61** | **0.43** | **0.41** | **xx** | **–** | **–** | **x** | **xxx** | **xxx** | **x** | **x** | **x** | **–** |
| BA-2-B-M* | 11.29 | 11.27 | 0.02 | 0.00 | – | x | – | – | x | x | x | – | x | xxx |
| BA-3-T* | 9.92 | 9.35 | 0.57 | 0.06 | – | x | – | – | x | x | x | – | x | xxx |
| BA-3-B-T* | 11.04 | 10.61 | 0.43 | 0.04 | – | x | – | – | x | x | x | – | x | xxx |
| **BA-3-B-N**** | **2.01** | **1.65** | **0.36** | **0.18** | **xx** | **–** | **–** | **x** | **xxx** | **xxx** | **x** | **x** | **x** | **–** |
| BA-3-M* | 11.35 | 10.12 | 1.23 | 0.11 | – | x | – | – | x | x | x | – | x | xxx |
| BA-4-T* | 7.75 | 6.75 | 0.99 | 0.13 | – | x | – | – | x | x | x | – | x | xxx |
| **BA-4-N**** | **0.45** | **< 0.10** | **0.45** | **1.00** | **xx** | **–** | **x** | **x** | **xxx** | **xxx** | **x** | **x** | **x** | **–** |
| BA-4-M* | 12.24 | 11.15 | 1.09 | 0.09 | – | x | – | – | x | x | x | – | x | xxx |
| BAM-1-2-T* | 9.85 | 9.54 | 0.31 | 0.03 | – | x | – | – | x | x | x | – | x | xxx |
| **BAM-1-N**** | **0.52** | **< 0.10** | **0.52** | **1.00** | **xx** | **–** | **x** | **x** | **xxx** | **xxx** | **x** | **x** | **x** | **–** |
| BAM-2-3-T* | 9.30 | 8.62 | 0.68 | 0.07 | – | x | – | – | x | x | x | – | x | xxx |
| **BAM-2-N**** | **0.99** | **0.66** | **0.33** | **0.33** | **xx** | **–** | **–** | **x** | **xxx** | **xxx** | **x** | **x** | **x** | **–** |
| **BAM-3-N**** | **–** | **–** | **–** | **–** | **xx** | **–** | **x** | **x** | **xxx** | **xxx** | **x** | **x** | **x** | **–** |

* Carbonate-rich layers; ** Dark clay-rich layers (bold); TC: Total carbon wt%; IC: Inorganic carbon wt%; TOC: Total organic carbon wt%; OCR: Organic carbon ratio (TOC/TC); I/S: illite-smectite mixed-layers; Sm: smectite; Plg: palygorskite; Py: pyrite; Qz: quartz; Ms.: muscovite; Pg: paragonite; Chl: Chlorite; Cal: calcite; Dol: dolomite. Mineral abundance expressed as number of X (XXX: very abundant, X: moderate abundance; x: presence).

turn, governs the precipitation/evaporation ratio, with salinity increasing with increasing aridity.

Therefore, variations in the chemical composition of the paleolake water and pore-sediment fluids would have had a significant impact on authigenic mineral alteration (Velde and Meunier, 2008), promoting clay interaction with saline fluids. As clays alter in saline water, Mg uptake can be an important factor for the reaction progress. Octahedral Al can be partially substituted by Mg and this cation can also enter in the interlayer positions. Deocampo et al. (2017) indicated that, in eastern African lakes, the formation of trioctahedral phases can be directly attributed to the authigenic alteration of minerals that is controlled by the sensitive reaction of clay minerals with the highly saline brines. Under the influence of a reducing environment, due to decaying organic matter and bacterial activity, clay minerals can also uptake $Fe^{2+}$. TEM-EDX analyses of illite-smectite suggested that both cations were incorporated in similar proportions to the octahedral sheet

(Table 1).

Andrade et al. (2018) indicated that in the organic rich-matter environment of mangroves, dissolved and colloidal $Fe^{2+}$ and $Fe^{3+}$ are abundant in the interstitial water and the variation of redox conditions in the sediments promote the formation of reactive Fe phases (oxyhydroxides and sulfides) in constant transformation, favoring silicate mineral reactions that drive the incorporation of Fe into the authigenic clays and its reduction under these reducing conditions. Octahedral cation changes due to Mg and $Fe^{2+}$ uptake increase clay layer negative charge (Deocampo, 2015). Octahedral layer charge increase favors the K uptake in clays specially from solutions unusually enriched in K. The weathering of detrital K-feldspars and muscovite, both minerals very abundant in the source area (the Internal Zone of the Betic Cordillera), can be an important source to provide potassium for its fixation transformation in clays (Meunier and Velde, 2004). Hydrological closure and evaporative concentration at the lake sector of Baza produced concentrations of dissolved $K^+$ in solution high enough to enhance the K uptake in clays (Deocampo and Jones, 2014), which together with the incorporation of Fe and Mg to the octahedral layer and Mg to the interlayer, pointed to a low temperature illitization due to the environmental conditions of the sediments.

XRD distinction between pure smectite and disordered (R0) smectite-rich I/S is essential to confirm the existence of the initial stage of illitization process. The XRD peak at 1.4 nm, swelling to 1.7 nm after EGC treatment (Fig. 5) may be interpreted either as pure smectite or as disordered (R0) smectite-rich I/S (Moore and Reynolds, 1997). Their distinction (and possible determination of illite layers percentage) needs to be carried out according to the positions of the small peaks near 0.85 nm and 0.567 nm in the EGC treated specimen, that is, the theoretical positions of (002) and (003) of EGC-treated smectite. If such positions correspond to the half and third part of (001), the (00*l*) orders are rational and hence smectite is pure. With the presence and increase of illite layers those peaks separate each other, approximating respectively to (001) and (002) of illite. Their position indicates the percentage of illite layers (Moore and Reynolds, 1997). Fig. 5 showed that in the lake samples those peaks are not in the theoretical positions of (002) and (003) of EGC treated smectite but represent a continuous between the positions of pure smectite and 30% of illite layers. Assuming the disordered nature of R0 I/S, with more than 50% smectite layers, the interpretation at lattice level of such phenomenon is not complicate; a minor amount of illitic layers is present among the major smectitic ones, in variable proportions from place to place, producing the sum of individual diagrams from pure smectite to ≈ 30% illite layers.

This situation is typical of the beginning of the diagenetic transformation of smectite to illite (Merriman and Peacor, 1999; Vazquez et al., 2014; 2016). The first step in this transformation is the beidellitization of smectite, which generates negative charge necessary to allow the incorporation of $K^+$ (Arostegui et al., 2019 and references therein). AEM analyses showed that the composition of the analyzed smectites and/or smectite-rich I/S is characterized by a significant substitution of Si by $Al^{IV}$ (Table 1), that is, the smectitic material is basically beidellitic. This beidellitic character could be already present in the original smectites, due to their origin from the pelitic metamorphic complexes of the Internal Zone of the Betic Cordillera (Drief and Nieto, 2000). The octahedral negative charge generated by the Mg and $Fe^{2+}$ uptake in the saline waters of the lake and the beidellitic substitution would provide clay layer negative charge enough to admit K incorporation in the interlayer, hence the beginning of a diagenetic low temperature illitization.

## 6. Conclusions

This paper addressed the effect of physical and chemical conditions of hypersaline lake environments with organic matter on the mineral transformations in sediments of the eastern part of the Guadix-Baza Basin (SE Spain). The most likely process responsible for crystallization of (R0) illite-smectite mixed layers (I/S) in the lake organic matter-rich sediments of the Guadix-Baza Basin was the authigenic mineral alteration of clay minerals during periods of hypersaline waters associated to climate variations and hydrological closure of the basin. Wet periods supplied abundant hydrolyzed detrital silicate minerals and plant fragments. Arid periods and hydrological closure and evaporative concentration produced concentrations of dissolved Mg and K. Reducing organic rich-matter environment favored the presence of reactive Fe phases and the incorporation of Fe into the authigenic I/S R (0). Furthermore, the inclusion of significant amounts of K would be related to the interaction with brines enriched in K. The amount of K in this phase revealed an initial stage of low temperature illitization due to the environmental conditions of the sediments. K-fixation was enhanced by layer charge increase due to Al-by-Mg and Fe substitution in the octahedral layer, perhaps favored by Fe reduction.

## Credit author statement

I.A. F.J.G.T., R.J.E. and J.J.M conducted field observations and sampling. I.A., J.J.M., R.J.E., and F.N. performed microscopic observations (SEM and TEM, mineralogical, textural, and chemical analyses) and interpreted the X-ray diffractograms. All the authors discussed the analytical results and prepared the manuscript.

## Declaration of Competing Interests

The authors declare that they have no known competing financial interests or personal relationships that could have appeared to influence the work reported in this paper.

## Acknowledgements

This work has been financed by research projects PGC2018-094573-B-I00 and TASCUB (RTI2018-100737-B-I00) from the MCIU-AEI-FEDER, and research groups RNM-325 and RNM-179 of the Junta de Andalucía. We acknowledge the suggestions and comments from two anonymous reviewers and from the editor (Dr. M.V. Villar). María del Mar Abad is especially recognized for helping with the HRTEM and for being able of providing us the AEM analyses during the COVID-19 lockdown. The “Centro de Instrumentación Científico-Técnica of the Universidad de Jaén” is aknowledged for the use of the PANalytical Empyrean diffractometer and the Merlin Carl Zeiss electron microscope. The use of the PANalytical X'Pert Pro diffractometer of the “Departamento de Mineralogía y Petrología, Universidad de Granada, Spain” is also acknowledge. The access to the HAADF FEI TITAN G2 microscope and the Philips CM20 (STEM) microscope was facilitated by the “Centro de Instrumentación Científica of the Universidad de Granada”. The “Instituto de Recursos Naturales y Agrobiología of Sevilla, CSIC” is acknowledged for provide organic carbon analyses.

## References

Andrade, G.R.P., Cuadros, J., Partiti, C.M.S., Cohen, R., Vidal-Torrado, P., 2018. Sequential mineral transformation from kaolinite to Fe-illite in two Brazilian mangrove soils. Geoderma 309, 84–99.

Arostegui, J., Arroyo, X., Nieto, F., Bauluz, B., 2019. Evolution of clays in cretaceous marly series (Álava Block, Basque Cantabrian Basin, Spain): Diagenesis and detrital input control. Minerals 9 (40), 1–24.

Cliff, G., Lorimer, G., 1975. The quantitative analysis of thin specimens. J. Microsc. 103, 203–207.

Cuadros, J., Andrade, G., Ferreira, T.O., de Moya Partiti, C.S., Cohen, R., Vidal-Torrado, P., 2017. The mangrove reactor: fast clay transformation and potassium sink. App. Clay Sci. 140, 50–58.

Deocampo, D.M., 2004. Authigenic clays in East Africa: Regional trends and paleolimnology at the Plio-Pleistocene boundary. Olduvai Gorge, Tanzania. J. Paleolimnology 31, 1–9.

Deocampo, D.M., 2015. Authigenic clay minerals in lacustrine mudstones. Geol. Soc. Am. Spec. Pap. 515 (SPE515-03).

Deocampo, D.M., Jones, B.F., 2014. Geochemistry of saline lakes. In: Holland, H.D., Turekian, K.K. (Eds.), Treatise on Geochemistry, Second edition. vol. 7. Elsevier,

Oxford, pp. 437–469.
Deocampo, D.M., Cuadros, J., Wing-Dudek, T., Olives, J., Amouric, M., 2009. Saline lake diagenesis as revealed by coupled mineralogy and geochemistry of multiple ultrafine clay phases: Pliocene Olduvai Gorge, Tanzania. Am. J. of Sci. 309 (9), 834–868.
Deocampo, D.M., Berry, P.A., Beverly, E.J., Ashley, G.M., Jarrett, R.E., 2017. Whole-rock geochemistry tracks precessional control of Pleistocene lake salinity at Olduvai Gorge, Tanzania: a record of authigenic clays. Geology 45, 683–686.
Drief, A., Nieto, F., 2000. Chemical composition of smectites formed in clastic sediments. Implications for the smectite-illite transformation. Clay Miner. 35 (4), 665–678.
Drief, A., Martínez-Ruiz, F., Nieto, F., Velilla, V., 2002. Transmission electron microscopy evidence for experimental illitization of smectite in K-enriched seawater solution at 50 C and basic pH. Clay Clay Miner. 50, 746–756.
Folk, R.L., 2005. Nannobacteria and the formation of framboidal pyrite: textural evidences. J. Earth Syst. Sci. 114, 369–374.
García-Romero, E., Suárez, M., 2010. On the chemical composition of sepiolite and palygorskite. Clay Clay Miner. 58, 1–20.
García-Tortosa, F.J., Alfaro, P., Galindo Zaldívar, J., Sanz de Galdeano, C., 2008. Glacis geometry as a geomorphic marker of recent tectonics: the Guadix-Baza Basin (South Spain). Geomorphology 125, 517–529.
García-Tortosa, F.J., Alfaro, P., Gibert, L., Scott, G., 2011. Seismically induced slump on an extremely gentle slope (< 1°) of the Pleistocene Tecopa paleolake (California). Geology 39, 1055–1058.
Gibert, L., Ortí, F., Rosell, L., 2007. Plio-Pleistocene lacustrine evaporites of the Baza Basin (Betic Chain, SE Spain). Sediment. Geol. 200, 89–116.
Haberland, C., Gibert, L., Jurado, M.J., Stiller, M., Baumann-Wilke, M., Scott, G., Mertz, D.F., 2017. Architecture and tectono-stratigraphic evolution of the intramontane Baza Basin (Betics, SE-Spain): Constraints from seismic imaging. Tectonophysics 709, 69–84.
Hay, R.L., Guldman, S.G., Mathews, J.C., Lander, R.H., Duffin, M.E., Kyser, T.K., 1991. Clay mineral diagenesis in core KM-3 of Searles Lake, California. Clay Clay Miner. 39, 84–96.
Kasina, M., Bock, S., Wurdemann, H., Pudlo, D., Picard, A., Lichtschlag, A., Marz, C., Wagenknecht, L., Wehrmann, L.M., Vogt, C., Meister, P., 2017. Mineralogical and geochemical analysis of Fe-phases in drill-cores from the Triassic Stuttgart Formation at Ketzin $CO_2$ storage site before $CO_2$ arrival. Environ. Earth Sci. 76, 161. https://doi.org/10.1007/s12665-017-6460-9.
Love, L.G., 1967. Early diagenetic iron sulfide in recent sediments of the Wash (England). Sedimentology 9, 327–352.
Love, L.G., Al-Kaisy, A., H, T., Brockley, H., 1984. Mineral and organic material in matrices and coatings of framboidal pyrite from Pennsylvanian Sediments, England. J. Sediment. Petrol. 54, 869–876.
MacLean, L.C.W., Pray, T.J., Onstott, T.C., Brodie, E.L., Hazen, T.C., Southam, G., 2007. Mineralogical, chemical and biological characterization of an anaerobic biofilm collected from a borehole in a deep gold mine in South Africa. Geomicrobiol J. 24, 491–504.
Maclean, L.C.W., Tyliszczak, T., Gilbert, P.U.P.A., Zhou, D., Pray, T.J., Onstott, T.C., Southam, G., 2008. A high-resolution chemical and structural study of framboidal pyrite formed within a low-temperature bacterial biofilm. Geobiology 6, 471–480.
Merriman, R.J., Peacor, D.R., 1999. Very low-grade metapelites: Mineralogy, microfabrics and measuring reaction progress. In: Frey, M., Robinson, D. (Eds.), Low-Grade Metamorphism. Blackwell Science, Oxford, pp. 12–87.
Meunier, A., Velde, B., 2004. Illite: Origin, Evolution and Metamorphism. Springer, New York.
Millot, G., 1964. Géologie des argiles. Alterations. Sédimentologie. Géochimie. Bull Groupe Français Argiles. 14-9, 165–166.
Moore, D.M., Reynolds, R.C.J., 1997. X-Ray Diffraction and the Identification and Analysis of Clay Minerals. 378 p. Oxford Univ. Press, New York.
Nieto, F., Ortega-Huertas, M., Peacor, D.R., Arostegui, J., 1996. Evolution of illite/smectite from early diagenesis through incipient metamorphism in sediments of the Basque-Cantabrian Basin. Clay Clay Miner. 44, 304–323.
Noël, V., Boye, K., Kukkadapu, R.K., Bone, S., Pacheco, J.S.L., Cardarelli, E., Janot, N., Fendorf, S., Kenneth, H., Williams, K.H., John, R., Bargar, J.R., 2017. Understanding controls on redox processes in floodplain sediments of the Upper Colorado River Basin. Sci. Total Environ. 603-604, 663–675.
Post, J.L., 1978. Sepiolite deposits of the Las Vegas, Nevada area. Clay Clay Miner. 26, 58–64.
Renaut, R.W., 1993. Zeolitic diagenesis of late Quaternary fluviolacustrine sediments and associated calcrete formation in the Lake Bogoria Basin, Kenya Rift Valley. Sedimentology 40, 271–301.
Sánchez-Roa, C., Jiménez-Millán, J., Abad, I., Faulkner, D.R., Nieto, F., García- Tortosa, F.J., 2016. Fibrous clay mineral authigenesis induced by fluid-rock interaction in the Galera fault zone (Betic Cordillera, SE Spain) and its influence on fault gouge frictional properties. Appl. Clay Sci. 134, 275–288.
Singer, A., Stoffers, P., 1980. Clay Mineral diagenesis in two East African lake sediments. Clay Miner. 15, 291–307.
Suan, G., Rolleau, L., Mattioli, E., Suchéras-Marx, B., Rousselle, B., Pittet, B., Vincent, P., Martin, J.E., Léna, A., Spangenberg, J.E., Föllmi, K.B., 2013. Palaeoenvironmental significance of Toarcian black shales and event deposits from southern Beaujolais, France. Geol. Mag. 150, 728–742.
Velde, B., Meunier, A., 2008. The Origin of Clay Minerals in Soils and Weathered Rocks. Springer, Heidelberg.
Vera, J.A., 1970. Estudio estratigráfico de la Depresión de Guadix-Baza. Bol. Geol. Min. 81, 429–462.
Weaver, C.E., Beck, K.C., 1977. Miocene of the S.E. United States: a model for chemical sedimentation in a peri-marine environment. Sediment. Geol. 17, 234.